Proceedings of the ASME 2010 3rd Joint US-European Fluids Engineering Summer Meeting and 8th International Conference on Nanochannels, Microchannels, and Minichannels
FEDSM-ICNMM2010
August 1-5, 2010, Montreal, Canada

FEDSM-ICNMM2010-30724

AUTOMATIC PARTICLE IMAGE VELOCIMETRY UNCERTAINTY QUANTIFICATION

Benjamin H. Timmins
Department of Mechanical and Aerospace Engineering
Utah State University
Logan, Utah 84322
ben.timmins@aggiemail.usu.edu

Barton L. Smith
Department of Mechanical and Aerospace Engineering
Utah State University
Logan, Utah 84322
barton.smith@usu.edu

Pavlos P. Vlachos
Department of Mechanical Engineering
Virginia Polytechnic Institute and State University
Blacksburg, Virginia, 24061
pvlachos@vt.edu

ABSTRACT

A method to estimate the uncertainty of each vector in Particle Image Velocimetry measurements by estimating the parameters which contribute to errors in the computed velocity field is discussed. These parameters include particle image diameter, particle density, particle displacement, and velocity gradient. After PIV processing, our code "measures" these parameters and an estimate of the velocity uncertainty is made for each vector in the flow field.

NOMENCLATURE

Δt	Time difference between images
Δx	Particle displacement between images
$b_{\Delta t}$	uncertainty of the time difference
$b_{\Delta x}$	uncertainty of the displacement
b_k	Systematic uncertainty estimate
D_{true}	The true displacement
d_τ	Particle image diameter estimate
$d_{\tau_{\text{true}}}$	True Particle image diameter
d_p	Particle image density estimate
N	Number of samples used to compute $\bar{x}$
r	The average displacement computed
r_{high}	The upper limit of the uncertainty estimate
r_{low}	The lower limit of the uncertainty estimate
s_x	Computed standard deviation of a sample
U_r^+	The upper combined uncertainty limit
U_r^-	The lower combined uncertainty limit
$\bar{U}_r^+$	The upper combined average uncertainty limit
$\bar{U}_r^-$	The lower combined average uncertainty limit
u	The x component of velocity
u_{true}	The true x component of velocity
$\mathbf{v}$	Velocity vector containing all components
v	The y component of velocity
w	The z component of velocity

1 Introduction

Numerical simulations, including Computational Fluid Dynamics (CFD), are used extensively in engineering for aerodynamics of aircraft and vehicles, hydrodynamics of ships, power plant modeling, turbomachinery, cooling of equipment, modeling blood flow through veins and arteries, and more [1]. Before these simulation results can be used, they must first be validated by comparison to experimental data or analytic solutions. With the exception of a few simple flows, analytic solutions are not available. The full-field

velocity data provided by Particle Image Velocimetry (PIV) makes it an obvious choice for velocity validation measurements. PIV has the ability to provide instantaneous two- or three-component velocity fields which point measurement techniques, such as hot wire anemometry or Laser Doppler Velocimetry, can not. In numerical simulation validation, it is crucial to know the uncertainty for both the experimental and numerical data. A failure to do so can result in inaccurate models, flawed test results, and inefficient designs.

The uncertainty of a PIV measurement is a very complex function of several parameters [2]. These parameters include, but are not limited to, particle image diameter, particle displacement, density, and velocity gradients. While there has been extensive study of the impact of these parameters on PIV uncertainty, it is exceedingly rare to see them employed in a PIV uncertainty analysis. The nature of the impact of these parameters on the uncertainty is such that the uncertainty varies in space and time, so any attempt to determine the global uncertainty of data set post-priory is either impossible or is doomed to be very conservative.

In this paper, we present an effort to develop a framework to estimate the uncertainty of every PIV vector based on the measured flow as well as the raw image data. We begin by estimating the uncertainty of a publicly-available PIV code as a function of several known error sources. Our code (which is added to the PIV code) measures the parameters that are known to influence uncertainty. Once these parameters have been quantified, an estimate of the velocity uncertainty is made for each velocity vector in space and time. The influence of these parameters on uncertainty is determined from data gathered from synthetic images of known flow fields.

In summary we will:

1. Identify contributors to PIV error. For the purpose of this paper, we have selected these contributers:
    - Particle Size
    - Particle Density
    - Shear
    - Displacement
2. Generate synthetic images for flows that contain varying amounts of each of these contributors. All correlation effects are included (various combinations of the parameters)
3. Compute vector fields from the synthetic images and compare them to the known solution to find the errors as a function of each of the parameters. These form the basis for the uncertainties
4. Add the capability of estimating particle size and density as well as flow shear to the PIV code. (All PIV codes already estimate displacement)
5. Add the capability of coupling these estimates with the uncertainty information to determine the uncertainty for each vector.

1.1 PIV Algorithms

It is important to make the distinction between PIV software and a PIV algorithm. The PIV algorithm consists of a specific series of operations which are carried out on arrays of digital image pixel intensities. These pixel arrays are a representation of an area of fluid flow which contain seed particles that are illuminated by a light source. Examples of these operations include Fourier-based cross correlation, gaussian subpixel displacement estimators, windowing, multipass, etc. The logistics of data storage, manipulation, and implementation of the specific operations in order describe PIV software. If two instances of PIV software use the same algorithm, they must produce identical results. An understanding of the distinction between PIV algorithms and software is vital when considering the application of the results from any PIV study. When duplicating a published PIV result with a different algorithm, one will not be able to identically match the results. Also note that PIV processing with nearly any software requires the user to make dozens of choices on the algorithm features as well as the order in which they are executed. As a result, even with the same software, it is unlikely that two users will use identical algorithms.

1.2 Uncertainty Estimates for Specific PIV Algorithms

The purpose of this study is an attempt to quantify the uncertainty of PIV-computed velocity vectors automatically. It is not the intent of this study to prove the superiority of one PIV algorithm over another. The original intent of this study was to produce a universal uncertainty model which could be distributed with any PIV software. By looking at the PIV Challenge results [3, 4, 5] it is clear that this cannot be accomplished. These studies show that various PIV algorithms have different errors for identical input. It is also apparent that different algorithms are more sensitive to certain image parameters than others, such as shear, par-

ticle diameter, and density. Because of this, a single PIV uncertainty model for all algorithms cannot provide realistic results.

To further demonstrate the need for individualized uncertainty values for each PIV algorithm, synthetic images are processed using LaVision's DaVis 7.2.2 and PIVadvance, which was developed at Virginia Tech [6, 7, 8]. The average error of velocity vectors from a uniform flow based on subpixel displacement only was computed for flows processed by the two PIV algorithms. The images processed with DaVis used 3 passes with the first pass interrogation regions 64 pixels square and the final pass 16 pixels square. A circular window was applied to each pass. The images are processed with PIVadvance using a Multigrid Standard Cross Correlation routine with gaussian windowing and three passes similar the one ones used by DaVis. Not only do the velocity error values differ, but the shape and sign of the error curves are significantly different between the different algorithms (see Figure 1).

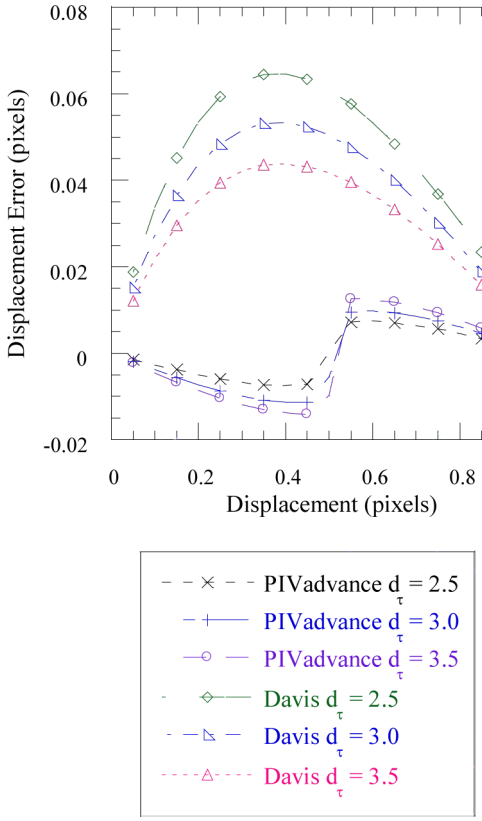

Figure 1. Average subpixel displacement error as computed by DaVis 7.2.2 and PIVadvance for different diameters d at a particle image density of 0.0293 particles/pixel^2.

2 Uncertainty Estimation

Using a 1-D equation for clarity, the calculation of velocity in PIV measurements come from the assumption that

$$u = \frac{dx}{dt} \approx \frac{\Delta x}{\Delta t}. \tag{1}$$

The uncertainty of u can come from both the displacement Δx and the time increment Δt. Using the Taylor Series Method for uncertainty propagation [9] the combined uncertainty estimate for the velocity assuming that the uncertainty of Δx and Δt are not correlated is

$$u_u^2 = \left(\frac{\partial u}{\partial \Delta x}\right) b_{\Delta x} + \left(\frac{\partial u}{\partial \Delta t}\right) b_{\Delta t} \tag{2}$$

where $b_{\Delta x}$ and $b_{\Delta t}$ are the uncertainty estimates of Δx and Δt. The uncertainty of Δt is small enough that it is assumed negligible so the uncertainty of u becomes proportional to the computed displacement $b_{\Delta x}$. Equation 2 simplifies to

$$u_u = \left(\frac{1}{\Delta t}\right) b_{\Delta x}. \tag{3}$$

The Monte Carlo Method (MCM) for determining the combined uncertainty assumes a Probability Density Function (PDF) for each input variable. The values of these variables are randomly chosen according to the assumed distribution and the solution is computed from the data reduction equation. The calculation is repeated until the standard deviation is converged [9] which is the uncertainty estimate that includes all correlation effects.

The data reduction equation for PIV is given by its algorithm. The inputs to the data reduction equation are arrays of pixel intensities and the output is a vector. Pixel intensities in a single image are correlated with each other through particle image diameter, and density. The pixel intensities between image pairs are correlated with each other though particle displacement, shear, and rotation. For most PIV algorithms, it is not beneficial to develop an analytic expression of the data reduction equation. If an interrogation region were only 8 pixels square, the data reduction

equation becomes a function of $2(8)^2 = 128$ pixel intensity values. Because the data reduction equation is a function of many variables, all of which are correlated, a MCM to determine a combined uncertainty estimate is selected. The random variable in the MCM simulation is particle location, which is selected from a uniform distribution.

2.1 Generating the Uncertainty Surface

According to [2], the main sources of error in PIV are particle image density, in-plane loss, out-of-plane loss, particle diameter, particle displacement, and shear. In-plane loss and out-of-plane loss will be considered as a criterion to exclude data. The others sources of error will be the focus of the current study to estimate uncertainty values. A multipass PIV algorithm is used so only the subpixel displacement will be considered as contributing to the uncertainty value. This assumption was tested and found true 97% of the time. The effects of background noise are not included in the uncertainty surface because they are considered negligible compared to noise created by the FFT correlation [2] (the impact of image noise on the method's ability to quantify error inputs will be assessed). The uncertainty data given by [2] is not used as it is specific to the algorithm that was used to generate it.

For interrogation regions experiencing identical true displacements (made from synthetic images) the same vector is not always computed from interrogation region to interrogation region. Even though the data reduction equation is the same for each region, the inputs of pixel intensities differ. The pixel intensity arrays vary because particles are randomly distributed throughout the flow. Another difference arises because the Fourier-Based Cross-Correlation computation introduces noise into the correlation map [2] which is dependent on the input pixel intensity arrays. The distribution of these displacements is used to compute a 95% confidence interval (see Figure 2).

There exist unique upper, r_{high}, and lower, r_{low}, values of the precision uncertainty (since the distribution of PIV error is, in general, not symmetric) for each data point and a systematic uncertainty value b_k. The systematic uncertainty is computed as the difference between the true displacement D_{true} and the average computed displacement r. The precision uncertainty values are calculated by computing the area under the probability curve, and, since the curve is a histogram, integration is accomplished by summing the

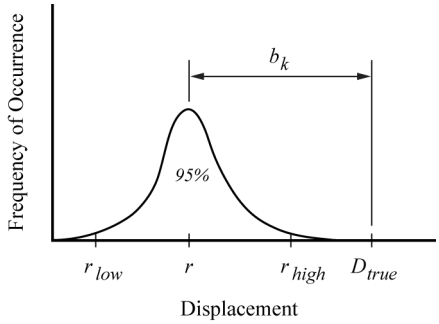

Figure 2. Theoretical histogram showing the distribution of computed displacements and the true displacement D_{true}. $\bar{x}$ is the average displacement that is calculated by the PIV algorithm. The value b_k is the systematic uncertainty value. $s_{\bar{x}_u}$ and $s_{\bar{x}_l}$ are the upper and lower bounds in which 95% of the data are contained

values. The lower limit r_{low} is the difference between r and the point at which the area under the curve is 2.5% of total area under the histogram. Similarly the upper bound r_{high} is difference between the point in which the area under the curve is 97.5% of the total area and r [9].

The combined uncertainty estimate for the lower uncertainty bar limit can be computed as Equation 4 and the upper bound as Equation 5.

$$U_r^- = \sqrt{r_{\text{low}}^2 + b_k^2} \tag{4}$$

$$U_r^+ = \sqrt{r_{\text{high}}^2 + b_k^2} \tag{5}$$

It should be noted that no assumptions have been made about the shape (PDF) or location of the displacement distributions. Although the b_k is considered a symmetric uncertainty value, it is represented as having a unique upper and lower bound with magnitudes that are identical.

It is often desired to compute time statistics for PIV velocity measurements. An estimate of the uncertainty on the mean of a velocity vector can be computed as

$$\bar{U}_r^- = \left(1.96\frac{s_x}{\sqrt{N}}\right)^2 + \sum_{i=1}^{N}\left(U_{r_i}^-\right)^2 \tag{6}$$

$$\bar{U}_r^+ = \left(1.96\frac{s_x}{\sqrt{N}}\right)^2 + \sum_{i=1}^{N}\left(U_{r_i}^+\right)^2 \tag{7}$$

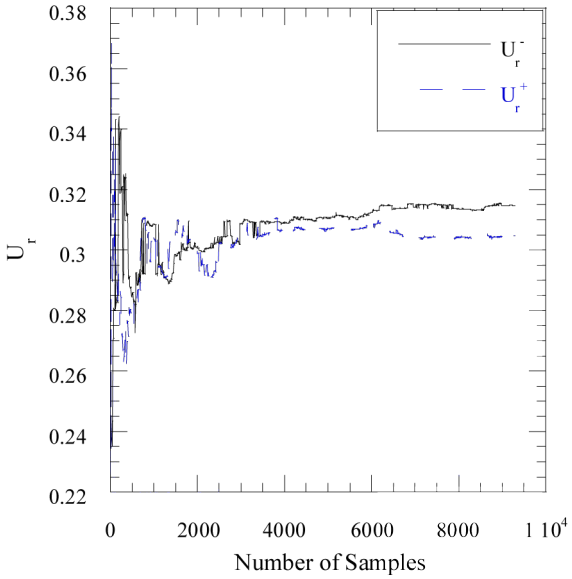

Figure 3. Values of U_r^- and U_r^+ for different numbers of samples used to compute them

where s_x is the standard deviation of the velocity at a point in space and $U_{r_i}^-$ and $U_{r_i}^+$ are the uncertainty values for each velocity measurement that was used to compute s_x.

The data are recorded for multiple particle image diameters, densities, displacements, and velocity gradients creating an input parameter space which is defined in Table 2.1. The number of data points to be used was determined after a convergence study was performed. The results of a convergence study are shown in Figure 3. All permutations of each parameter combination is computed using roughly $10,000$ vectors for each data point. The data points are post-processed using a median filter [13]. Vectors which are identified as outliers are removed. By generating $10,000$ vectors for each data point, a sufficient number of points remain after the spurious vectors are removed.

This data creates a 4-D uncertainty surface. Some of the results are presented by holding two variables constant and varying the other two. Figure 4 shows U_r^+ for no gradient and -1.00 pixel displacement. From Figure 4 it is seen the uncertainty estimate is almost constant with diameter and density with the exception of small particle image diameters and low particle density. Figure 5 shows U_r^+ for 2.50 pixel particle image diameter and 0.00195 particle/pixel^2 density. From Figure 5 it is seen the uncertainty estimate is a weak function of displacement, but is heavily sensitive to shear.

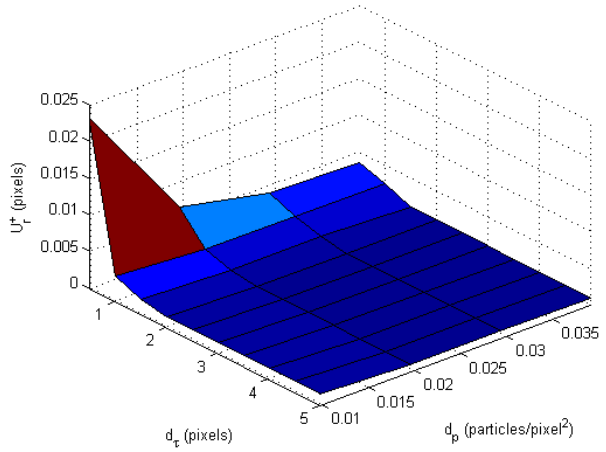

Figure 4. U_r^+ surface for 0.00 gradient and -1.00 pixel displacement

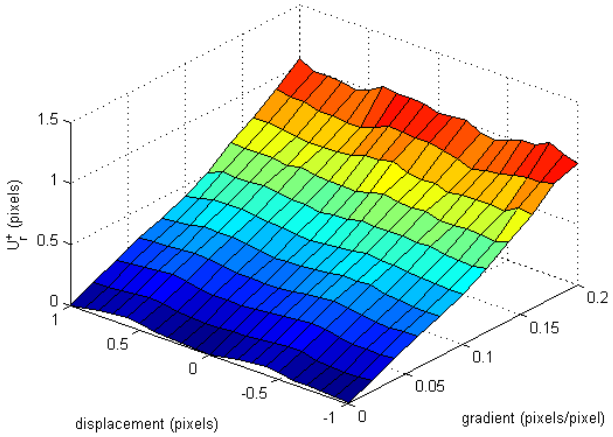

Figure 5. U_r^+ surface for 2.50 pixel particle image diameter and 0.00195 particle/pixel^2 density.

3 Results

The estimated uncertainty based on the uncertainty surface was computed from flows having a uniform profile, a linear profile, a Couette-Poiseuille flow, a Burger's Vortex, and a laminar separation bubble [10]. Information on how these were generated can be found in Appendix A.

Input Parameter	Lower Limit	Upper Limit	Step size
Particle Image Diameter (pixels)	0.5	5.0	0.5
Particle Image Density (particles/pixels^2)	0.0098	0.0391	0.0098
Particle Image Displacement (pixels)	-1.0	1.0	0.1
Gradient (pixels/pixel)	0.00	0.20	0.02

Table 1. Table showing the range of the computed uncertainty estimates

Flow Type and Correlation	no noise (u/v)	PCO Sensicam QE noise (u/v)	FastCam noise (u/v)
Uniform Flow SCC	78.0% / 66.4%	61.5% / 56.7%	71.0% / 61.9%
RPC	94.1% / 87.9%	89.6% / 83.0%	87.3% / 77.0%
Linear Profile SCC	93.0% / 44.5%	92.8% / 44.7%	93.0% / 41.0%
RPC	95.5% / 41.8%	96.1% / 42.7%	95.6% / 39.4%
Couette-Poiseuille SCC	93.3% / 42.8%	92.5% / 45.1%	92.8% / 39.6%
RPC	95.9% / 44.5%	97.4% / 49.6%	95.8% / 41.4%
Burger's Vortex SCC	78.5% / 77.4%	78.4% / 77.5%	78.1% / 77.0%
RPC	86.2% / 83.5%	88.2% / 85.4%	86.0% / 83.1%
PIV Challenge '05 case B SCC	72.3% / 33.6%	- / -	- / -
RPC	89.9% / 69.0%	- / -	- / -

Table 2. Table showing the percentage of computed velocity vector components which contain the true value within the error bounds (ex. $u - U_r^- < u_{true} < u + U_r^+$). Normally distributed background noise is added to to the images with a mean of zero and variance equal to a percentage of the maximum possible pixel intensity (256 for an 8-bit camera).

3.1 Assessing the Appropriateness of the Error Bars

The appropriateness of the estimated uncertainty is determined by examining the percentage of calculated vectors which contain the true value within their error bounds. If all error sources have been taken into account, the uncertainty bars on 95% of the computed vectors should contain the true value. This percentage was computed for all flows and three background noise levels (for cases for which images were generated) including no noise, and noise levels corresponding to two common cameras (as described in the Appendix). Differing levels of background noise are included to test the results of [2], that it is negligible, and to make the synthetic images more realistic. The results are tabulated in Table 2 for both the standard cross correlation (SCC) and robust phase correlation (RPC) methods. Each flow analyzed contained $16,129$ vectors with the exception of the PIV Challenge '05 case B which has 3608 vectors. Each image was post-processed using a median filter and spurious vectors were removed. In all cases, no more than 0.6% of the vectors were removed by the median filter.

From Table 2, most cases are in the neighborhood of 95% for the dominant flow direction (which is the x direction for the liner profile and Couette-Poiseuille Flows). Numbers significantly lower than 95% indicate that either 1) an error source parameter, such as shear, has been estimated incorrectly or 2) and error source has been neglected.

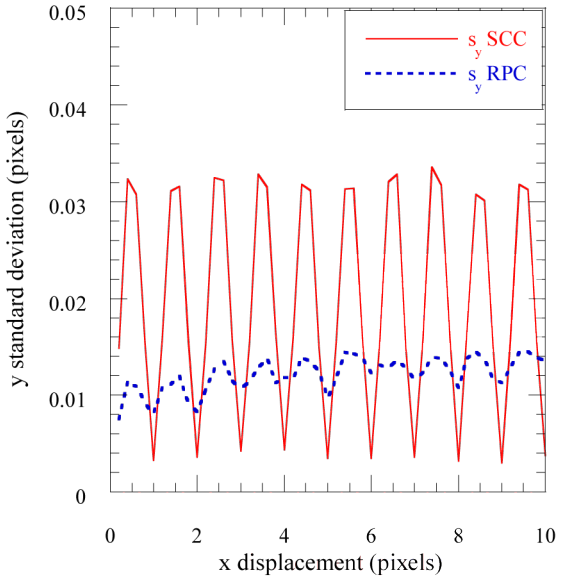

Figure 6.

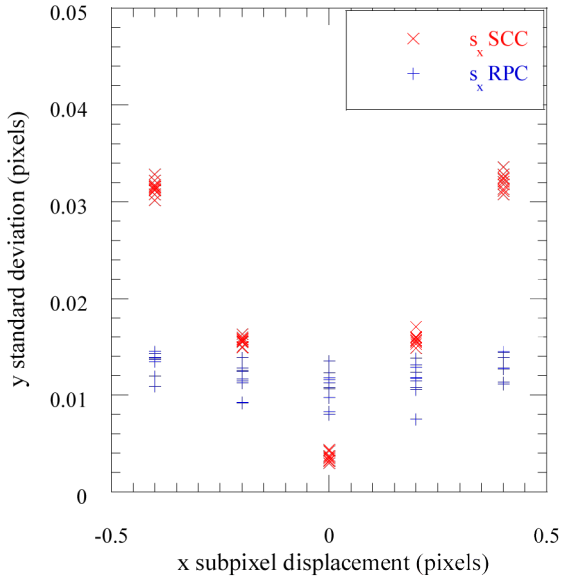

Figure 7.

Since the two cases with $v = 0$ have inappropriate uncertainty bars on the v components, 1-D flow was further investigated to see if the u and v velocity components within the same interrelation region are correlated with each other. To do this, 50 synthetic image pairs were created with displacements ranging from 0.2 pixels to 10.0 pixels along the x-axis with $v = 0$. Background noise was added to each to approximate that of the PCO CCD camera as described in the Appendix. Each image pair produced 3969 vectors and was post-processed with a median filter to remove spurious vectors. Less than 1.5% of vectors were removed in post-processing. Figure 6 shows the standard deviation of the y displacement component (which should be zero) for both the SSC and RPC methods.

The periodic behavior appears similar to displacement peak locking. By removing all integer displacements from the data in Figure 6, the same data are shown as a function of subpixel displacement only (Figure 7).

It is apparent that the for the SCC method, there is noise induced on a velocity component proportional to the subpixel displacement on the other component. For the RPC method the amount of noise induced on a velocity component is less than that of the SCC method, but it is still present and actually increases as the displacement of the orthogonal component increases. The uncertainty surface produced for this study did not account for this effect. This may explain the poor uncertainty estimate on the zero v cases. In fact, this effect will degrade performance in any case where all other error sources are insignificant. This also explains why the RPC method, which suffers from this problem to a much smaller extent than the SSC method, provides better uncertainty results then the SSC method even though they each have their own unique uncertainty surface. For the method presented in this paper to be successful, a fifth dimension would need to be added to the uncertainty surface which accounts for the displacement of the orthogonal velocity component.

Lastly, we note that adding image noise had very little impact on any of the results. This is consistent with the conclusions of [2] and validates the decision to not include noise in the uncertainty surface.

3.2 Uncertainty Field Computations Compared with Error

The first flow analyzed is that of a uniform velocity field. The data was created with particle image diameters equal to 2.5 pixels, and a particle image density of 0.0293 particles/pixel^2. This case serves as a base line of a simple flow with two significant velocity components and no gradient. The uniform displacement is set such that there is a 3.268 pixel displacement along the x-axis, and a 5.876 pixel displacement along the y-axis. A plot of the velocity field, and the computed width of the uncertainty bars,

$\sqrt{\left(U_{r_x}^-\right)^2+\left(U_{r_y}^-\right)^2}+\sqrt{\left(U_{r_x}^+\right)^2+\left(U_{r_y}^+\right)^2}$, is shown in Figure 8. It can be seen in Figure 8b that the uncertainty levels are generally small for a flow with zero gradient, but that regions of larger uncertainty do exist due to other factors. It is also clear that these regions, in most cases, correspond to regions of larger error. This is the desired performance of the method.

For a linear velocity profile (constant gradient of 0.02 pixels/pixel) with particle image diameter equal to 2.5 pixels, and particle image density of 0.0293 particls/pixel^2, the velocity field and the width of the uncertainty bars are shown in Figure 9a-b. The majority of the uncertainty bars have the same size, since shear will dominate the uncertainty estimate. The fluctuations in the uncertainty bar width are most likely due to errors in the estimate of the velocity gradients $\partial u/\partial y$ and $\partial v/\partial x$. An error in the computed velocity vector will be amplified during numerical differentiation. Again, however, note the strong correlation between regions of large uncertainty and regions of large uncertainty.

Combined Couette-Poiseuille flow, which has a varying gradient, is also analyzed with a particle image diameter equal to 2.5 pixels and a particle image density of 0.0293 particls/pixel^2. The velocity field and the width of the uncertainty bars are shown in Figure 10a-b. As expected, the width of uncertainty bars increased in areas of higher shear and decrease in areas of low shear when the uncertainty due to displacement becomes significant. A plot showing the u velocity profile is shown in Figure 11 with 95% confidence uncertainty bars and the true value of u.

A Burger's Vortex, which is a rotating flow, is also analyzed. The particle image diameter is 2.5 pixels, and particle image density is 0.0195 particls/pixel^2. A plot of the velocity field, and the computed width of the uncertainty bars are shown in Figure 12a-b. The gradients ($\partial u/\partial y$ and $\partial v/\partial x$) in this flow are small and constant. Because of the small gradients, the uncertainty due to the subpixel displacement, which is sinusoidal, is significant. The fluctuations in the uncertainty bar width appear periodic are due to the effect of the sub pixel estimation uncertainty at that location.

For the PIV Challenge '05 case B data the major source of error comes from shear, the effects of which dominate the uncertainty estimates. A plot of the velocity field, and

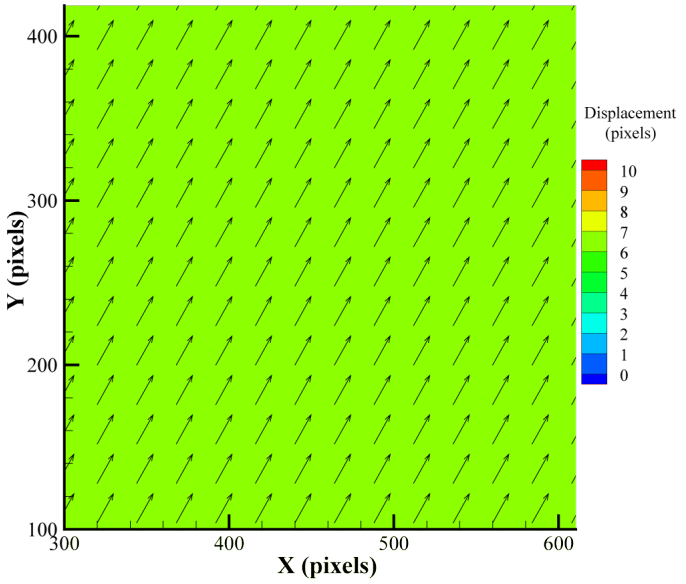

(a)

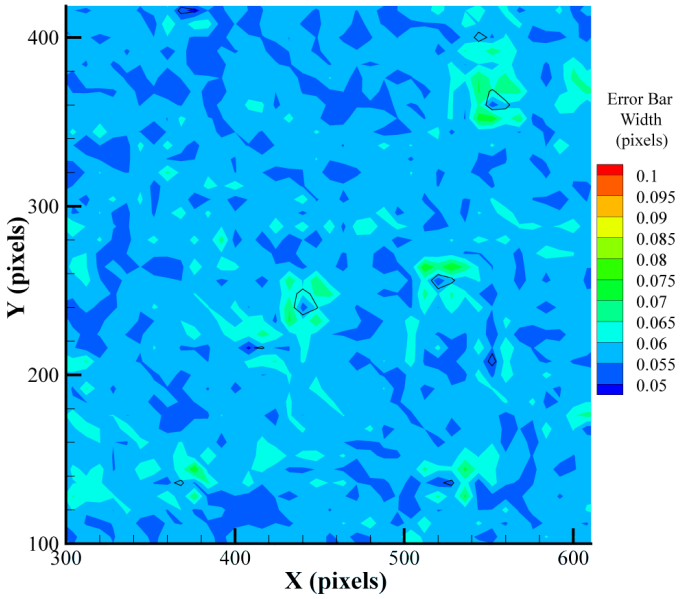

(b)

Figure 8. (a) Plot of the calculated displacement of the uniform profile velocity field with no background noise computed with the RPC method. (b) Plot of the width of the uncertainty bar associated with each displacement vector and superimposed error contour. The error level contours are 0.0, 0.05, and 0.1 pixels.

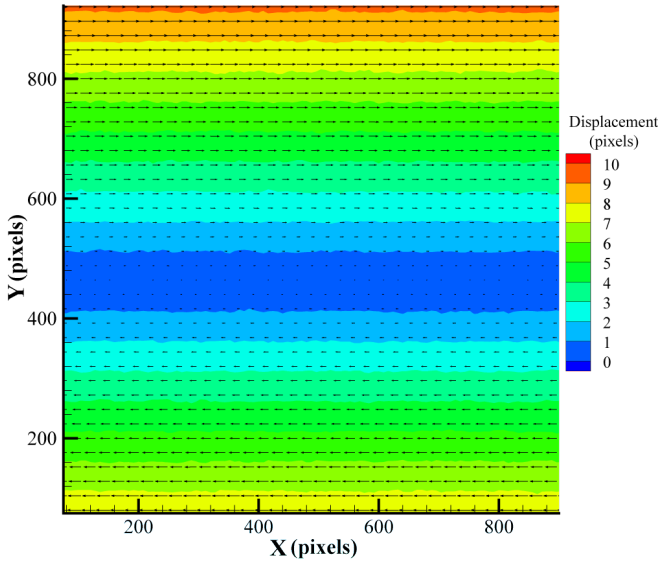

(a)

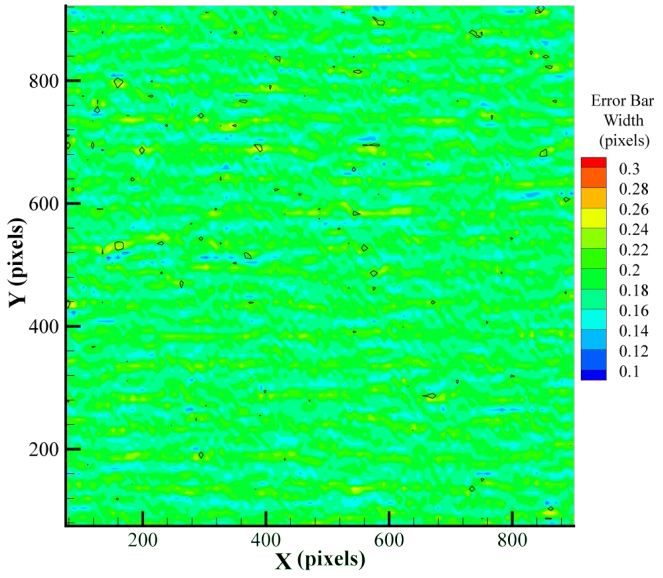

(b)

Figure 9. (a) Plot of the calculated displacement of the linear profile velocity field with no background noise as computed with the RPC method. (b) Plot of the width of the uncertainty bar associated with each displacement vector and superimposed error contour. The error level contours are set at 0.0, 0.1, and 0.2 pixels.

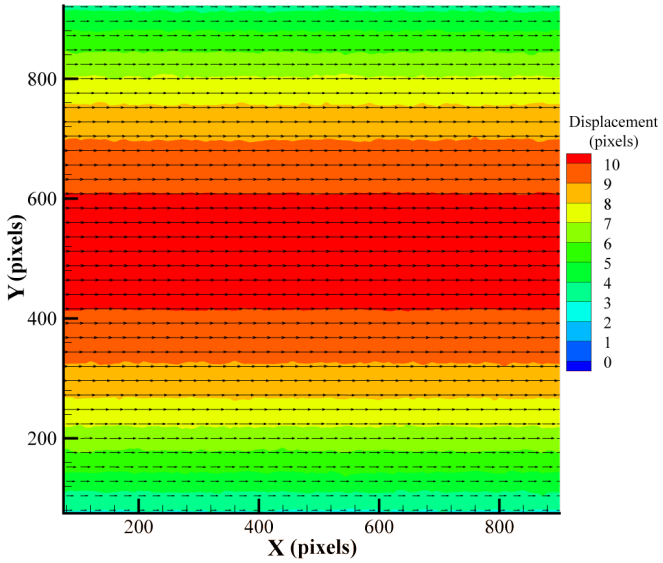

(a)

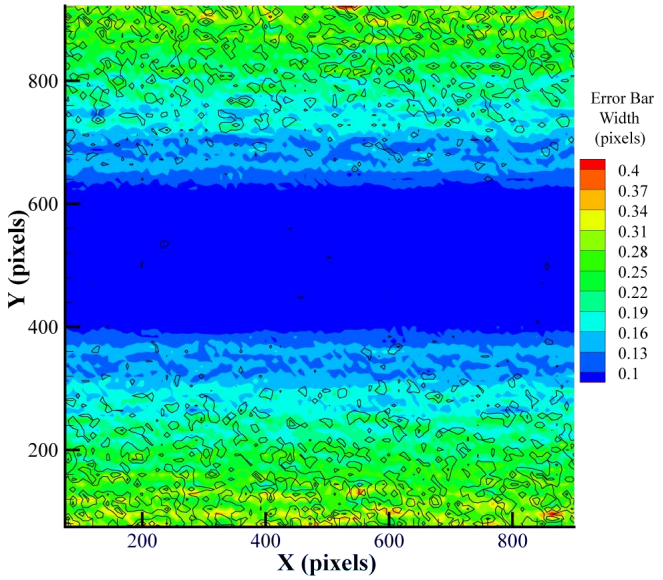

(b)

Figure 10. (a) Plot of the calculated Couette-Poiseuille flow field displacement with no background noise as computed by the RPC method. (b) Plot of the width of the uncertainty bar associated with each displacement vector and superimposed error contour. The error level contours are 0.0,0.05, and 0.1 pixels.

the computed width of the uncertainty bars are shown in Figure 13a-b. It is seen that the predicted uncertainty values are higher in areas of larger error.

The importance of individual uncertainty estimates can easily be seen when a plot is made showing the uncertainty bar width as a percentage of the local velocity. This was done for the combined Couette-Poiseuille flow (Figure 14) and the PIV Challenge '05 case B flow (Figure 15). Channel flow is often thought of as having high uncertainty near the wall. Some of this velocity field may have an ac-

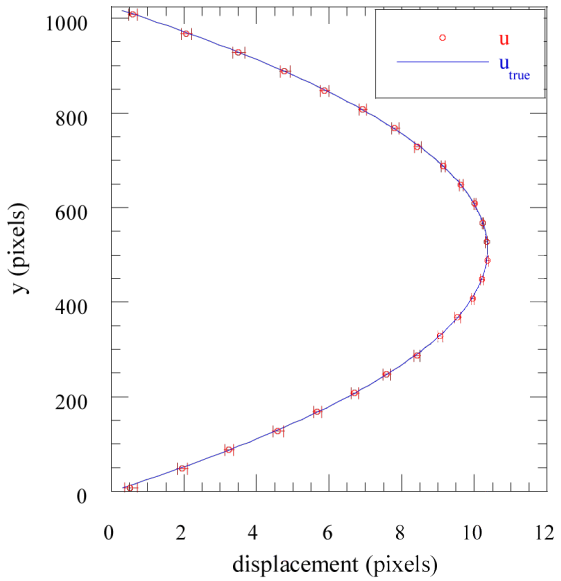

Figure 11. Comparison of the computed value of u and its 95% uncertainty bar at constant $x = 31$mm for a Couette-Poiseuille flow which has 10% background noise.

ceptable level of uncertainty. Using a single uncertainty value for the entire flow (which is common) obscures the fact that some of the data are much better that others.

It is seen in Figure 15 that for a flow which appears to have a reasonable velocity profile (Figure 13a), the uncertainty for local velocity values can reach unacceptable levels. If a single uncertainty value were defined for the entire flow region, it would need to be large enough to capture the vectors with the largest uncertainty. Such an approach often would label PIV velocity fields with an uncertainty high enough to cause the case to be discarded. If individual uncertainty values are assigned to each local vector, then each vector can be individually assessed based on its uncertainty level. Since the uncertainty estimates generated do not capture 95% of the true values, the uncertainty estimate as a percentage of local velocity is an underestimation. Because of this Figure 14 and Figure 15 are expected to overestimate the local accuracy of PIV.

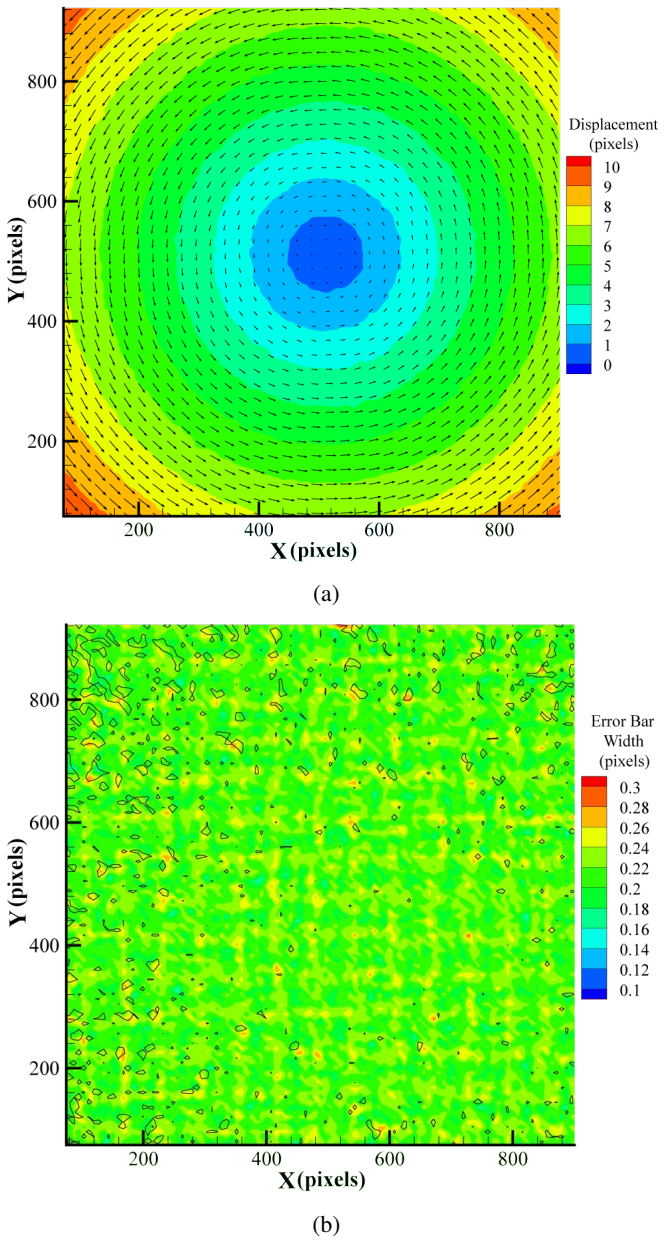

Figure 12. (a) Plot of the calculated Burger's Vortex flow field displacement with no background noise as computed by the RPC method. (b) Plot of the width of the uncertainty bar associated with each displacement vector and superimposed error contour. The error level contours are 0.0, 0.1, and 0.2 pixels.

4 Conclusions

A method to compute local PIV velocity vector uncertainty is demonstrated. The method focused on traditionally accepted image parameters which are thought to produce error in PIV measurements. Namely: particle image diameter, particle density, particle displacement, and local shear. It is shown that an estimate of the velocity uncertainty can be made for every velocity vector in a flow field. The results shown are specific to the PIVadvance algorithm,

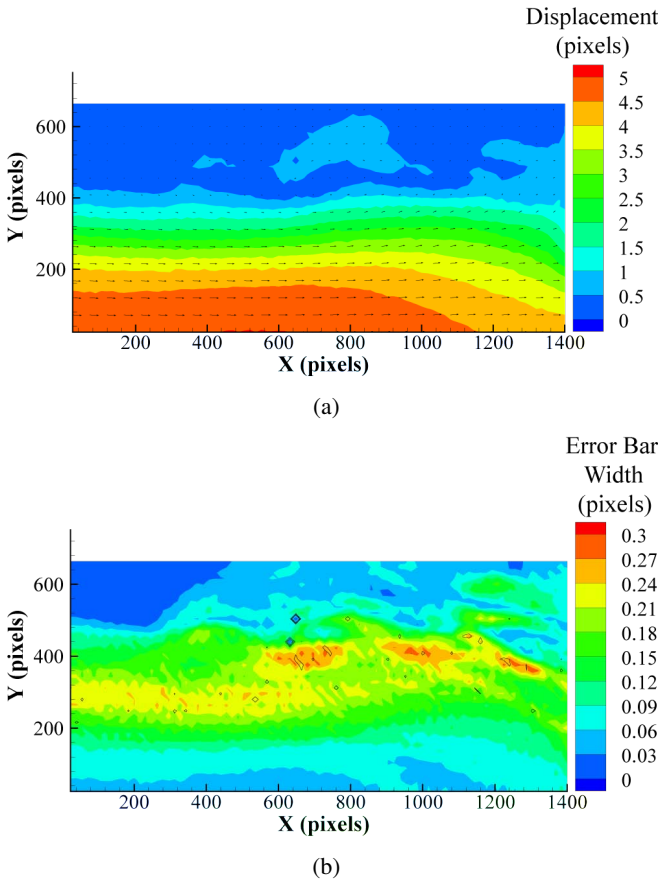

Figure 13. (a) Plot of the PIV Challenge '05 case B flow field displacement as computed by the RPC method. (b) Plot of the width of the uncertainty bar associated with each displacement vector in the DNS flow field with superimposed error contours. The error level contours are set at 0.0, 0.1, 0.2, and 0.3 pixels.

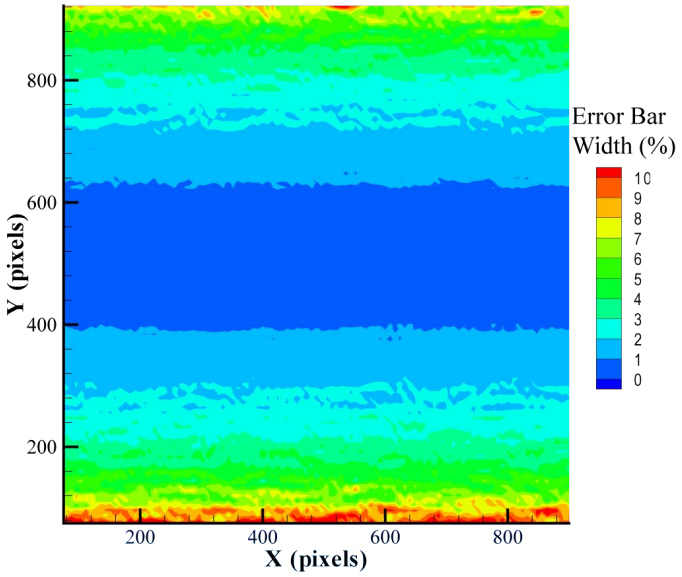

Figure 14. A plot of the local uncertainty estimate as a percentage of local velocity for the combined Couette-Poiseuille flow.

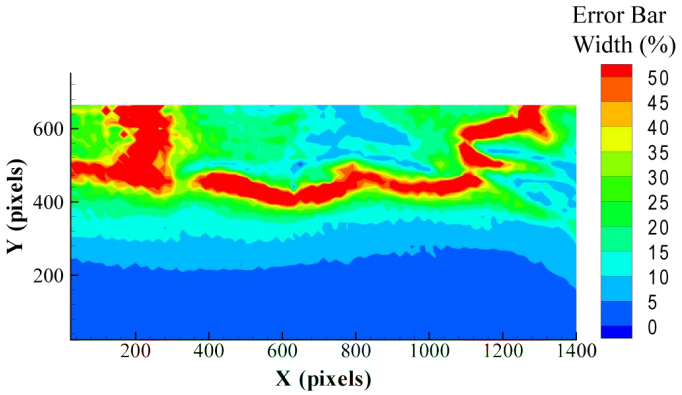

Figure 15. A plot of the local uncertainty estimate as a percentage of local velocity for PIV Challenge '05 case B flow field.

although similar results could be made with other algorithms. The uncertainty estimate is less sensitive to particle image diameter, density and displacement (with some exceptions) but highly sensitive to shear.

This method tended to grossly under predict the uncertainty levels for one dimensional flows for the component with no displacement. It was suggested that this is because motion in one direction introduces noise in the orthogonal direction. The method generally under predicts the the uncertainty levels for all two dimensional flows analyzed. Motion induced noise is different from dynamic range in that it affects accuracy even when particle displacements are very small or similar magnitudes. The level of uncertainty caused by the motion induced noise is dependent on the PIV algorithm chosen. Further work is needed to better understand and quantify the effect of motion induced noise.

The importance of local velocity uncertainty estimation has been demonstrated. For flows which have "good" looking velocity fields, the local uncertainty can reach unacceptable levels. With local uncertainty values, areas of the flow can be assessed and removed when uncertainty levels are too high, while other sections of flow may be retained and used. This is a significant improvement over global uncertainty estimates.

While the method presented has serious flaws that need

to be addressed and is probably not yet general enough for wide spread use, the potential and importance of local uncertainty estimates for PIV has been amply demonstrated.

ACKNOWLEDGMENT

This work has been supported by the United States Department of Energy through the Idaho National Laboratory's LDRD Project NE-156. Special thanks to John Charonko for providing PIVadvance, the PIV algorithm used, and Satyapraksh Karri for his help with the robust gradient estimation method.

REFERENCES

[1] H K Versteeg and W Malalasekera. *An Introduction to Computational Fluid Dynamics the Finite Volume Method*. Pearson, Edinburgh England, 2007.

[2] Markus Raffel, Chris E. Willert, Steve T. Wereley, and Jurgen Kompenhans. *Particle Image Velocimetry*. Springer-Verlag, Berlin Heidelberg, 1998.

[3] M. Stanislas, K. Okamoto, and C. Kaehler. Main results of the first international piv challenge. *Measurement Science and Technology*, 14:R63–R89, 2003.

[4] M. Stanislas, K. Okamoto, C. Kaehler, and J. Westerveel. Main results of the second international piv challenge. *Experiments in Fluids*, 39:170–191, 2005.

[5] M. Stanislas, K. Okamoto, C. J. Kaehler, J. Westerweel, and F. Scarano. Main results of the third international piv challenge. *Experiments in Fluids*, 45:27–71, 2008.

[6] A. Eckstein and P.P. Vlachos. Digital particle image velocimetry (dpiv) robust phase correlation. *Measurement Science and Technology*, 20:055401, 2009.

[7] A. Eckstein and P.P. Vlachos. Assessment of advanced windowing techniques for digital particle image velocimetry (dpiv). *Measurement Science and Technology*, 20:075402, 2009.

[8] A. C. Eckstein, J. Charonko, and P. Vlachos. Phase correlation processing for dpiv measurements. *Experiments in Fluids*, 45:485–500, 2008.

[9] Hugh W. Coleman and W. Glenn Steele. *Experimentation, Validation, and Uncertainty Analysis for Engineers*. John Wiley and Sons, Hoboken, NJ, 2009.

[10] M. Stanislas, K. Okamoto, C. J. Kahler, J. Westerweel, and F. Scarano. Main results of the third international PIV challenge. *Experiments in Fluids*, 45:27–71, 2008.

[11] F. White. *Viscous Fluid Flow*. McGraw-Hill, New York, NY, 2006.

[12] Akira Ogawa. *Vortex Flow*. CRC Press, Boca Raton, Florida, 1993.

[13] J. Westerweel and F. Scarano. Universal outlier detection for piv data. *Experiments in Fluids*, 39:1096–1100, 2005.

[14] Satyapraksh Karri, John Charonko, and Pavlos P. Vlachos. Robust wall gradient estimation using radial basis functions and proper orthogonal decomposition (pod) for particle image velocimetry (piv) measured fields. *Measurement Science and Technology*, 20:1–14, 2009.

[15] J Westerweel. Efficien detection of spurious vectors in particle image velocimetry data. *Experiments in Fluids*, 16:236–247, 1994.

Appendix A: Synthetic Image Generation

Using "Synthetic Images" based on known flow data (from analytical solutions or numerically computed flow fields) makes it possible to know the exact solution, and true error, for specific cases. A synthetic image is an artificial image of seed particles in a known velocity field. To generate these images, an algorithm was produced which follows the method discussed in [2].

We study five flows ranging from simple to complex: uniform flow, constant gradient, Couette-Poiseuille flow between plates, Burgers Vortex flow, and Direct Numerical Solution (DNS) for a laminar separation bubble from the 2005 PIV challenge [10].

A uniform velocity flow can be created by displacing all particles by the same specified magnitude for each velocity component. Mathematically it can be expressed as

$$\mathbf{v} = \begin{bmatrix} u \\ v \\ 0 \end{bmatrix}. \tag{8}$$

The uniform velocity flow field allows for study of PIV errors without gradients, rotation, and no out of plane loss.

The linear velocity profile (constant gradient) is de-

fined as

$$\mathbf{v} = y\left(\frac{du}{dy}\right) + \begin{bmatrix} u \\ 0 \\ 0 \end{bmatrix}. \tag{9}$$

The linear velocity profile allows the study of velocity calculations in the presence of shear without rotation and out of plane loss.

The combined Couette-Poiseuille flow is a laminar one-dimensional flow driven by a constant pressure gradient and moving upper wall with a no slip boundary condition at each wall. The flow field can be expressed as

$$\frac{u}{U} = \frac{1}{2}\left(1+\frac{y}{h}\right) + P\left(1-\frac{y^2}{h^2}\right), \quad P = \left(-\frac{dp}{dx}\right)\frac{h^2}{2\mu U} \tag{10}$$

where U is the velocity of the upper wall, and h is the half distance between plates [11]. The velocity vector then becomes

$$\mathbf{v} = \begin{bmatrix} u \\ 0 \\ 0 \end{bmatrix}. \tag{11}$$

The Couette-Poiseuille flow maintains a constant profile in a one-dimensional flow flied. By generating synthetic images from this flow field, the effects of non-constant shear can be examined without out-of-plane motion of the PIV algorithm.

A Burgers Vortex is a vortex model which assumes the fluid is steady, axis-symmetric, with small axial gradients of physical quantities. The flow velocity is described by

$$\frac{V_\theta}{V_{\theta b}} = \frac{R_{eb}}{2\left(1-e^{-R_{eb}/2}\right)}\frac{r}{b}, \quad R_{eb} = -\frac{bV_{rb}}{\nu_t} \tag{12}$$

$$\frac{V_r}{V_{rb}} = \frac{r}{b} \tag{13}$$

where b is the radius of the vortex, and V_{rb} and $V_{\theta b}$ are cylindrical components of velocity at $r = b$ [12]. Converting to cartesian coordinates

$$\mathbf{v} = \begin{bmatrix} V_r cos(\theta) - V_\theta sin(\theta) \\ V_r sin(\theta) + V_\theta cos(\theta) \\ 0 \end{bmatrix}. \tag{14}$$

Producing synthetic images that follow this flow field allow the study of the effects of rotating flow fields without out of plane motion on the PIV algorithm.

Background noise was added to each image at three different levels. The first level is zero noise, which is intended to give a best case scenario. The second noise level is meant to approximate the actual noise level in the PCO sensicam QE 12 bit CCD camera. To approximate the noise produced when recording images with this camera 100 image pairs are taken of air with no seed particles illuminated by a New Wave Research Solo PIV III ND-Yag Laser dual cavity laser. A histogram of the pixel intensities is generated to show the noise distribution. The histogram x-axis is normalized by the maximum pixel intensity (4095), and the y-axis is normalized by the total number of pixels recorded. The normalized histogram is fitted with a normal distribution:

$$y(x) = Ae^{-\frac{(x-\mu)^2}{2\sigma^2}}, \tag{15}$$

with average $\mu = 1.011e^{-2}$ and standard deviation $\sigma = 5.96e-4$. Random samples are then taken from this normal distribution and added to each image to simulate the background noise of the Imager Intense camera. The third noise level is meant to approximate the actual noise of the Photron FastCam APX RS 10 bit CMOS camera. Following the same procedure that was used for the second noise level, 100 image pairs are taken of air with no seed illuminated by a Photonics ND-YLF single cavity laser. A histogram is made and normalized in the same manner as the second noise case and fitted with a normal distribution of mean $\mu = 2.834e^{-3}$ and standard deviation $\sigma = 3.55e^{-3}$. This normal distribution is then randomly sampled to produce background noise for the third case. The normalized histograms from these cameras are seen in Figure 16.

Appendix B: Image Parameter Quantification

To use these uncertainty estimates, image parameters need to be quantified for non-synthetic data. The easiest

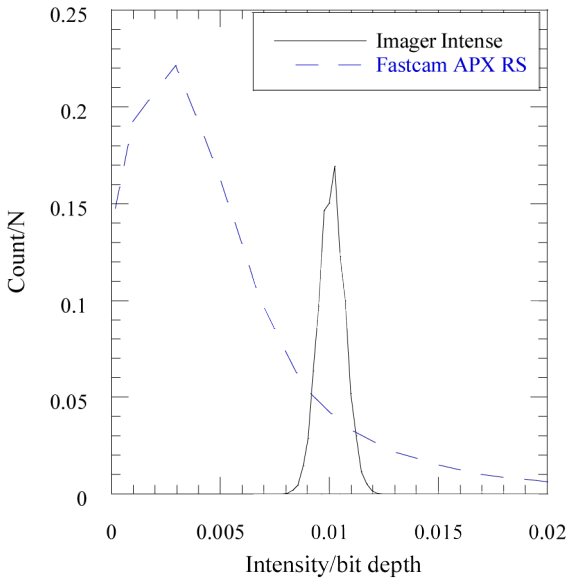

Figure 16. Normalized histogram of background noise from LaVision Imager Intense CCD and Photron FastCam APX RS CMOS cameras.

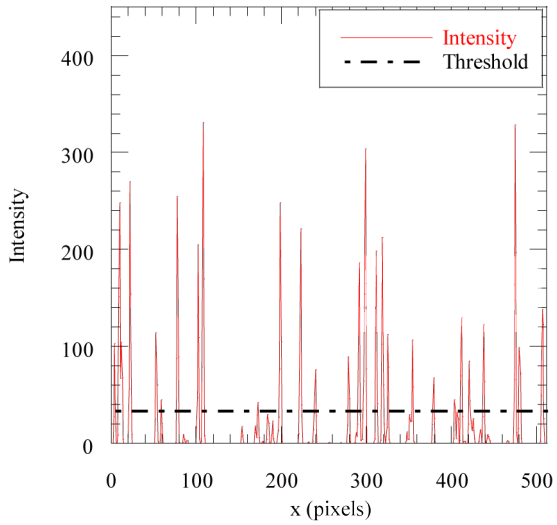

Figure 17. A singe row added to the proceeding and following rows of pixel intensity. Based on this singe row the algorithm computed the particle image diameter such that the relative error $[\mathrm{abs}(\mathrm{d}_{\tau\mathrm{true}} - \mathrm{d}_{\tau})/\mathrm{d}_{\tau\mathrm{true}}]100\%$ = 3.7%. The particle image density relative error was computed the same way to be 8.8%

parameter to quantify is displacement since the PIV algorithm already calculates this. Since it is the value of the subpixel displacement that creates error (assuming it is not a spurious vector), this quantity is stored for each vector. Depending on the algorithm used, this value can be determined by multiplying the velocity by Δt, then rounding the displacement to the neared integer pixel value, and taking the difference from the unrounded value.

The average particle image diameter and the average density are not as straight forward to determine. A preliminary method to automatically estimate the particle image diameter and density has been developed. Rows (or columns) of pixel intensities are selected from each PIV image pair. Each row is then averaged with the preceding and following rows. A plot of this is shown in Figure 17. Because real images will have background noise, a threshold value must be set such that background noise has a minimal impact on the diameter estimate. The peaks that extend above the threshold level are assumed to represent a particle image or cluster of multiple particle images. Peaks corresponding to multiple particle image clusters will be generally larger in magnitude and wider than those of single particle images. A gaussian curve is then fit to each peak above the threshold. The standard deviation, s_x, of the gaussian curve is computed for each assumed particle. The particle diameter is then estimated to be $2(1.6)(s_x)$, where the value 1.6 was empirically determined. An average particle image diameter is then from all gaussian fits. Other methods such as those used in Particle Tracking Velocimetry measurements may be used.

Using the gaussian fit for each assumed particle reduces the effect that the selected noise threshold has on the estimated d_τ which is seen in Figure 18. It is also seen that an average particle image predicted after sampling 30 rows becomes fairly constant. The exact values of each estimated particle image diameter varies randomly about a mean value. This is due to the random distribution of particles within each image. This scheme produces a very accurate estimate of the particle diameter for particles larger than 1 pixel, as shown in Figure 19.

As a first approximation of the background noise for an image, the threshold is set to the sum of the average pixel intensity of the image, $\bar{x}$, and the standard deviation of the pixel intensities s_x. To estimate the particle image density the image intensity values are filtered such that only pixel intensities larger than the threshold remain. The number of particles in the image is then estimated as the number of pixels in the filtered image divided by the projected area of

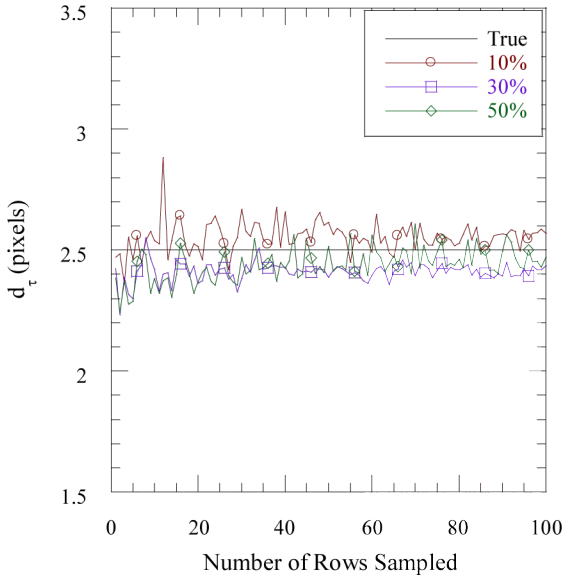

Figure 18. Particle image diameter, d_τ, is estimated with varying number of rows sampled. The noise threshold is set to 10%, 30%, and 50% of the maximum intensity.

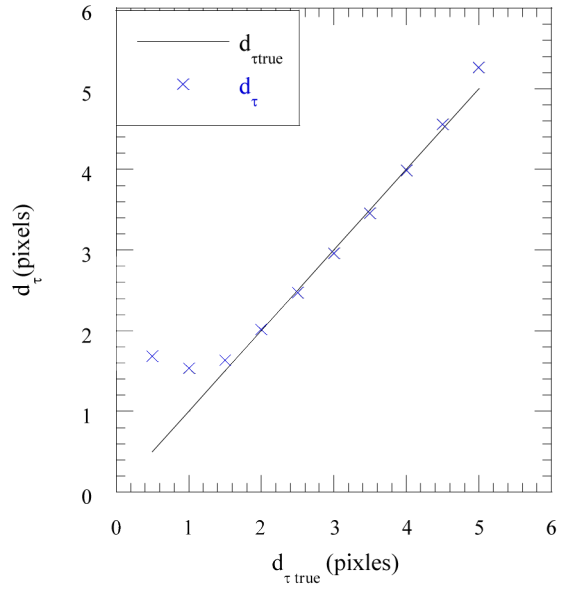

Figure 19. Particle image size algorithm results as a function of particle size.

a particle which is approximated by that of a circle

$$A_p = \frac{\pi (d_\tau)^2}{4}. \qquad (16)$$

The particle density can then be estimated by dividing the number of particles by the pixel area of the image. Experimental results indicate that this method tends to underestimate the particle image density. A correction factor of 1.32 is multiplied to the estimated particle image density estimate to provide a better estimate.

The fourth parameter that is needed for the uncertainty estimate is the velocity gradient. The method used to estimate the velocity gradient is the Robust Gradient Estimate Method described in [14] which has shown improvement in derivative estimates over other methods such as finite difference.

Effects of Noise on Parameter Quantification

The effects of noise on gradient estimation can be found in [14], and the effects of noise on displacement estimation can be found in [6, 7, 8]. To see the effects of noise on particle image diameter and density, three levels of background noise are investigated which are created from a normal distribution with zero mean and variance equal to 0%, 10%, and 20% of the maximum intensity value. A plot of the estimated diameter and density for the three noise levels is seen in Figure 21 and Figure 22. The uncertainty bars on the data points are based on a Student's t distribution with sample size of 4. As we can see the estimate of the particle image diameter remains accurate for the three levels of noise while the estimated particle image density rises with increased noise. The estimation of particle image density will be an area of future study.

From Figure 4 and Figure 5 it is concluded that the accuracy with which this method finds the particle image diameter and density will have little effect on the uncertainty estimate. The ability to accurately predict the uncertainty is most directly related to the accuracy that the gradient can be estimated.

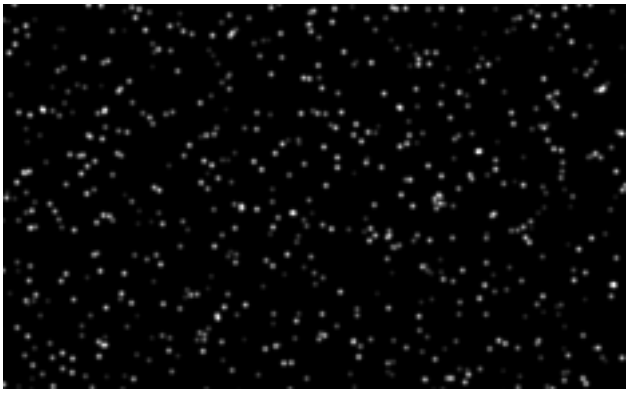

(a)

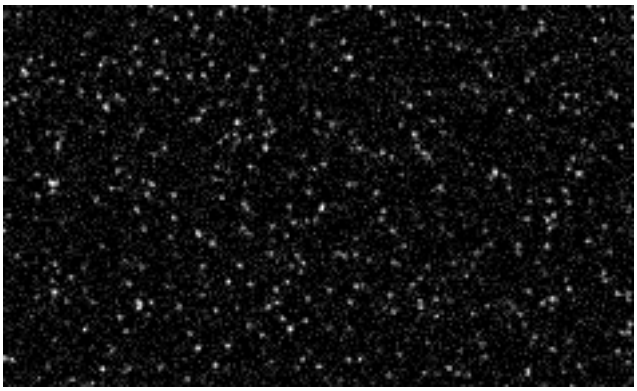

(b)

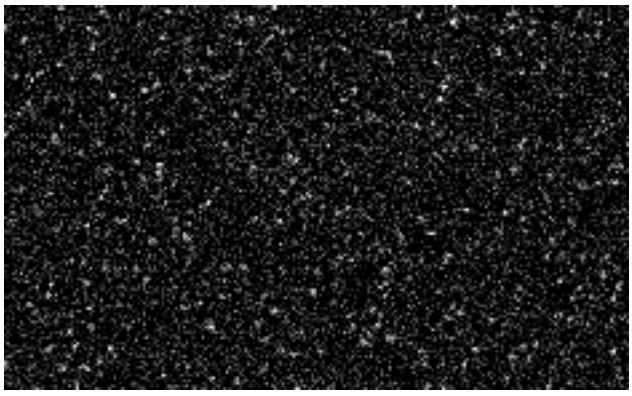

(c)

Figure 20. A section of an image with particle image diameters of 2.5 pixels, density 0.0192 particles/pixel^2 and (a) 0.0% background noise (b) 10.0% background noise (c) and 20.0% background noise.

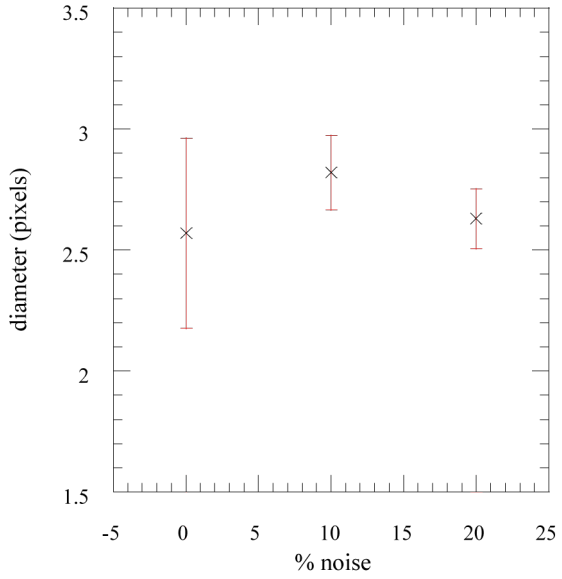

Figure 21. The effect of image background noise on the estimated particle image diameter. The actual value is 2.5 pixels. Error bars are computed from a Student's t distribution of 4 samples and a 95% confidence interval.

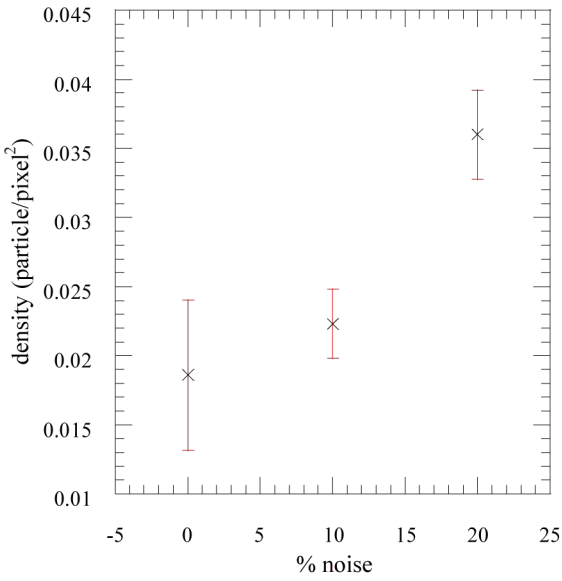

Figure 22. The effect of image background noise on the estimated particle image density. The actual value is 0.02. Error bars are computed from a Student's t distribution of 4 samples a 95% confidence interval.